THE JOURNAL OF PHYSICAL CHEMISTRY C
A JOURNAL OF THE AMERICAN CHEMICAL SOCIETY

pubs.acs.org/JPCC

Article

Probing Lattice Dynamics in Two-Dimensional Inorganic Pseudohalide Perovskites with Ultrafast Infrared Spectroscopy

Xiangyu Xing, Jiayi Li, John P. Breen, Jun Nishida, Hemamala I. Karunadasa,* and Michael D. Fayer*

Cite This: *J. Phys. Chem. C* 2022, 126, 10145−10158

Read Online

ACCESS | Metrics & More | Article Recommendations | Supporting Information

ABSTRACT: Dynamic lattice disorder in two-dimensional (2D) halide perovskites can play an important role in their optical properties through carrier/exciton−lattice interactions. Previously, the 2D halide−pseudohalide perovskite $(MA)_2Pb(SCN)_2I_2$ (MA^+ = methylammonium) was demonstrated to have a dynamically inhomogeneous lattice with structural evolution occurring on a picosecond time scale. Here, we have investigated two purely inorganic 2D perovskites, $Cs_2Pb(SCN)_2X_2$ (X = Br or I). 2D infrared (2D IR) and polarization-selective pump−probe (PSPP) experiments were used to study dynamics and the effects of changing the halide anions. The ^{12}CN stretching mode was used as the vibrational probe. The films were isotopically doped, ∼99% ^{13}CN, to avoid excessive IR absorption, heating, and vibrational excitation transfer. PSPP measurements were performed on thin films using the reflection geometry to improve the signal-to-noise ratio. The results showed that the ^{12}CN vibrational lifetime in $Cs_2Pb(SCN)_2X_2$ is significantly longer than that in $(MA)_2Pb(SCN)_2I_2$, and the lifetimes were essentially the same for Br and I analogues of $Cs_2Pb(SCN)_2X_2$. 2D IR spectroscopy is carried out to measure both spectral diffusion (structural evolution) and homogeneous dephasing of the inhomogeneously broadened CN stretch absorption line. The $Cs_2Pb(SCN)_2X_2$ 2D perovskites displayed substantially slower structural evolution compared to $(MA)_2Pb(SCN)_2I_2$. The spectral diffusion is independent of the halide anion. There is also significant homogeneous dephasing caused by the coupling of the CN stretch to lattice phonons. Our findings provide insights into lattice dynamics of inorganic 2D perovskites and lay a foundation for studies on their complex carrier/exciton−lattice interactions, of importance for applications in optoelectronic devices.

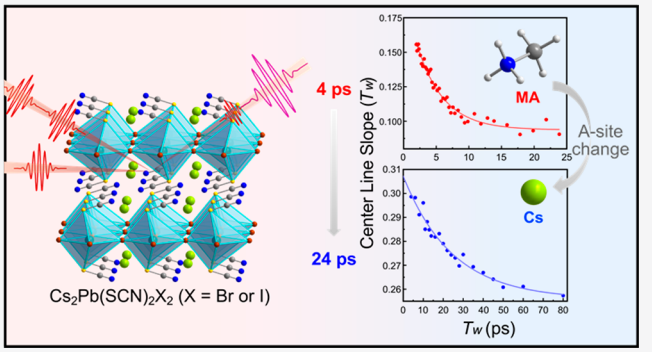

1. INTRODUCTION

Layered perovskites, known since the 1900s,[1] have re-emerged as a versatile class of two-dimensional (2D) materials for optoelectronics. They are promising candidates as components in photovoltaics,[2−4] light-emitting diodes,[5−9] and other photonic applications[10−14] due to a multitude of properties: strong light absorption and emission, shallow defect formation, and facile solution-state deposition methods. The larger band gap and higher exciton binding energy of 2D perovskites in comparison to their three-dimensional (3D) counterparts are a result of their reduced dimensionality,[1] whereas their increased stability has been attributed to the organic layers.[2] Figure 1 shows the 3D and 2D perovskite structures. The 2D perovskites have the general formula A_2BX_4. These structures are usually composed of corner-sharing $[BX_6]$ octahedra in layers separated by A-site cations. Here, A is typically an organic monovalent cation, B is a divalent metal cation, and X is a halide. In analogy to 3D pseudohalide perovskites[15] (e.g., $[(CH_3)_4N]Mn(N_3)_3$), the terminal halides of 2D perovskites can be replaced by pseudohalides (e.g., SCN^- and I_3^-) to afford mixed halide−pseudohalide perovskites.[16−19] One of the most important characteristics of 2D perovskites is their enormous structural tunability,[20] which can be achieved by X-site anion substitution, careful selection of A- and B-site cations, and morphology control.[19] By tailoring the structure of 2D perovskites, they may have a wide range of applications. A fundamental understanding of their structural dynamics is important for realizing the potential of 2D perovskites.

The underlying mechanisms of 2D perovskites' varied optical properties are not fully understood. Experimental and theoretical studies that increase our understanding can lead to rational design principles for particular applications of 2D perovskites. For example, the combination of moderate charge carrier mobility and long charge carrier lifetime in 3D lead halide perovskites has attained widespread interest, and the

Received: May 20, 2022
Revised: May 26, 2022
Published: June 10, 2022

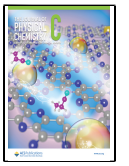

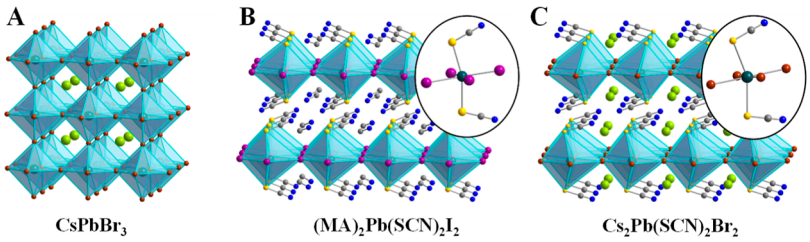

Figure 1. (A) Crystal structure of the 3D $CsPbBr_3$ perovskite. (B) Crystal structure of the 2D $(MA)_2Pb(SCN)_2I_2$ perovskite (MA—methylammonium). (C) Crystal structure of the 2D $Cs_2Pb(SCN)_2Br_2$ perovskite. Green, turquoise, brown, purple, yellow, gray, and blue spheres correspond to Cs, Pb, Br, I, S, C, and N atoms, respectively. Hydrogen atoms are omitted for clarity.

dynamic flexibility of the soft perovskite lattices is believed to facilitate stabilization of the charge carriers.[21] There has been a good deal of work investigating the lattice structural evolutions of lead halide perovskites, but most of the previous work has been confined to 3D perovskites.[22−29] Quan et al. studied the coherent phonon dynamics in various 2D perovskites by pump−probe transient absorption spectroscopy and found that organic cations can accelerate the dephasing rate of optical phonons and alter the vibrational relaxation processes because of their large anharmonicity.[30] Fast rotation of the organic cations in 2D perovskites has also been observed by Koegel et al. through high-energy resolution neutron scattering.[31] The dynamics of the A-site cations influence the optoelectronic properties of the perovskites mostly through indirect templating effects. Therefore, we sought to probe the dynamics of purely inorganic 2D perovskites, where the motion of the inorganic framework directly affects the optical and electronic properties.

In this study, we employ 2D infrared (2D IR) spectroscopy and other ultrafast nonlinear IR techniques to explore the lattice dynamics of thiocyanate-based 2D perovskites with the nitrile stretching mode used as the vibrational probe. Pseudohalide-based 2D perovskites have attained increased recent interest. Here, the longer pseudohalide ligands coordinate to the axial positions of the metal and effectively partition the inorganic sheets. Therefore, small cations (Cs^+ and MA^+) can be used for the A-site, instead of the larger organic cations more commonly employed to separate the inorganic sheets. The resulting extremely short interlayer distances afford various unique properties among 2D pseudohalide perovskites, including low excitonic binding energy (E_b), decreased band gap (E_g), and large pressure response (piezochromism).[17,32,33] Studies of $(MA)_2Pb(SCN)_2I_2$ thin films using 2D IR spectroscopy were performed previously.[34] The spectral diffusion, which measures structural fluctuations of the lattice variations that give rise to the inhomogeneously broadened CN stretch absorption band, was observed with a time constant of 4.1 ± 0.3 ps. The spectral diffusion was ascribed to thermal fluctuations that interconvert local and mesoscopic lattice configurations.

The organic−inorganic 2D perovskite $(MA)_2Pb(SCN)_2I_2$ was shown to be unstable to ambient moisture and moderate (50 °C) heat.[17] Recently, the all-inorganic 2D perovskites, $Cs_2Pb(SCN)_2Br_2$ and $Cs_2Pb(SCN)_2I_2$, have been reported to possess better stability compared to $(MA)_2Pb(SCN)_2I_2$.[35] All-inorganic perovskites typically lack suitable vibrational probes, and the CN stretch in these pseudohalide 2D perovskites opens up opportunities for exploring their distinct 2D framework fluctuations, which can shed light on the role of A- and X-site ions in the structural dynamics. The thin films of $Cs_2Pb(SCN)_2Br_2$ and $Cs_2Pb(SCN)_2I_2$ will be referred to as the Br^-- and I^--containing samples, respectively. 2D IR, polarization-selective pump−probe (PSPP), and Fourier-transform infrared (FT-IR) experiments were performed on these films. The experiments were conducted on the ^{12}CN stretch of the 1% $S^{12}CN^-$ in samples that were prepared with 99% $S^{13}CN^-$ to avoid vibrational excitation coupling between nearby SCN^- anions. The high-concentration CN stretch of $S^{13}CN^-$ shows a splitting as has been observed previously for $(MA)_2Pb(SCN)_2I_2$.[34] The reflection geometry PSPP experiments were used to measure the vibrational lifetimes of the CN stretch in the Br^- and I^- samples. Both lifetimes are substantially longer when the organic A-site cation is replaced by the inorganic Cs^+ cation. However, the lifetime is unchanged by the choice of the X-site anion. The 2D IR experiments show that the spectral diffusion is significantly slower when the A-site cation is Cs^+ rather than MA^+, but it does not depend on whether the X-site anion is Br^- or I^-, within experimental error.

2. EXPERIMENTAL METHODS

2.1. 2D Infrared Spectroscopy with Acousto-Optic Modulator Pulse Shaping. 800 nm pulses (~70 fs, 6 W, 3 kHz) are generated with a Ti:Sapphire oscillator/regenerative amplifier. A home-built optical parametric amplifier pumped by the 800 nm pulses was used to produce mid-IR pulses centered at ~2087 cm^{-1} with a ~90 cm^{-1} full width at half-maximum (FWHM) bandwidth. The 2D IR spectroscopic measurements were performed using a germanium acousto-optic modulator (AOM) pulse shaper.[36] A pulse sequence of three IR pulses (~160 fs), composed of two pump pulses with a temporal delay τ, followed by a probe pulse after a waiting time of T_w, was focused into the sample. The interactions of these three pulses with the sample induce a third-order nonlinear polarization, which gives rise to a fourth pulse, the vibrational echo, which is the signal. The time delay τ was controlled by the AOM pulse shaper, and a motorized delay stage was used to scan the time T_w between the two pump pulses and the probe pulse. The two pump pulses are collinear, and the probe pulse overlaps with the pump pulse at a crossing angle of ~16°. The resulting vibrational echo pulse propagates collinearly with the probe pulse, which is the local oscillator (LO) for heterodyne detection of the signal. The combined signal/LO is steered into a spectrograph and detected with a 32-pixel HgCdTe (MCT) array detector. The 2D IR spectra were obtained by performing two Fourier transforms. Scanning τ produces an interferogram at each frequency detected by the array detector. Fourier transformation of these interferograms gives the ω_1 axis (horizontal). The spectrograph takes the time domain echo/LO pulse into the frequency domain, which is an experimental Fourier transform, which gives the ω_3 axis

https://doi.org/10.1021/acs.jpcc.2c03516
J. Phys. Chem. C 2022, 126, 10145−10158

(vertical). The pulse shaper was used to control the phases of pulses 1 and 2, and a four-shot or eight-shot phase cycle was used to reduce scattered light interference with the signal.

At early T_w, the 2D line shape is elongated along the diagonal as the initial frequencies are significantly correlated with the final frequencies. As T_w proceeds, the frequencies become less correlated due to structural fluctuation, making the 2D line shape rounder. This change in shape is used to determine the normalized frequency−frequency correlation function (FFCF) using the center line slope (CLS) method.[37,38]

The normalized FFCF is the probability that the vibrational probe with a frequency at time $t = 0$ has the same frequency at a later time, averaged over all the frequencies in the inhomogeneously broadened absorption line shape. The complete FFCF is typically described with the Kubo model[36,39]

$$\mathrm{FFCF} = C_\omega(t)\langle \delta\omega(0)^2\rangle = \langle \delta\omega(t)\delta\omega(0)\rangle = \sum_i \Delta_i^2 \exp[-t/\tau_i] \quad (1)$$

where $C_\omega(t)$ is the FFCF and the frequency fluctuation, $\delta\omega(t) = \omega(t) - \langle\omega\rangle$, is the difference between the instantaneous frequency at time t and the average frequency, $\omega(t)$ and $\langle\omega\rangle$, respectively, while Δ_i and τ_i are the amplitude of the frequency fluctuation and the time constant of the ith decay pathway, respectively. If a pathway is in the motionally narrowed limit, $\Delta_i\tau_i \ll 1$, then it contributes to the homogeneous line width, $\Gamma = 1/\pi T_2$, which is the result of ultrafast fluctuations, that is, pure dephasing processes, as well as the vibrational lifetime and orientational relaxation. The homogeneous component is given by

$$\frac{1}{T_2} = \frac{1}{T_2^*} + \frac{1}{2T_1} + \frac{1}{3T_{or}}$$

where T_2 is the total homogeneous dephasing time, T_2^* is the pure dephasing time, T_1 is the vibrational lifetime, and T_{or} is the orientational correlation time. For the perovskite crystals, the lifetime is long and orientational diffusion does not occur. Therefore, the homogeneous contribution to the FFCF discussed below is all from pure dephasing.

Qualitatively, 2D IR works as follows. The first pulse labels the vibrational probes, the CN stretch of SCN^-, with their initial frequencies. The second pulse stores the information. During the time between the second and third pulses, T_w, the structures in the proximity of the probes evolve. The change in structures causes the interactions of the surroundings with probes to change, which changes the CN frequencies. The third pulse initiates the frequency readout, and the emitted echo pulse gives the final frequencies. As T_w is increased, there is more time for the structure and therefore the frequencies to change. The time dependence of the 2D spectrum reports on the time evolution of the frequencies and, thus, the time evolution of the perovskite structures that give rise to the inhomogeneously broadened CN absorption spectrum.

2.2. Near-Brewster's Angle Reflection Mode. To avoid resonant vibrational exciton coupling between adjacent CNs, the 2D IR and other experiments are conducted on 1% ^{12}CN, while the rest (99%) of the CNs are ^{13}CN. In addition, the perovskite films are very thin, with a thickness of tens of nanometers. While necessary, these factors result in a weak IR absorption of ∼1 mOD (0.001 absorbance). To enhance the 2D IR signal-to-noise ratio, the experiments are conducted in the near-Brewster's angle reflection geometry.[40,41] The information is carried by the modulation of the LO by the echo signal. When the incident angle on the sample of the probe pulse in the 2D IR pulse sequence is close to Brewster's angle, the LO amplitude is greatly diminished but the signal field is virtually unaffected. Thus, the signal modulation of the LO is considerably enhanced by a factor of 30−50. An incident angle of 53° was used to perform measurements on the perovskite thin films.

2.3. PSPP Spectroscopy. PSPP experiments were also conducted to investigate the vibrational lifetime and the anisotropy decay of the CN stretch of the SCN^- ions in the perovskite lattices. The temporal separation, t, between a single pump and probe pulse was scanned by the mechanical delay stage. The population and anisotropy decay curves can be extracted from the time-dependent pump−probe signal. The pump polarization is set at 45° by a half-wave plate and a polarizer, and the probe polarizer is set at 90° (vertical polarization), which corresponds to s-polarized light. A computer-controlled resolving polarizer is placed after the sample and is alternated between +45° and −45° relative to the pump polarization on alternate delay line scans to measure the parallel ($S_\parallel$) and perpendicular ($S_\perp$) signals, respectively.

Like the 2D IR experiments, the PSPP experiments were also performed in reflection to enhance the pump−probe signal. However, for the PSPP experiments, the incident angles were kept relatively small (probe incident angle = 18° and pump incident angle = 2°). A more detailed discussion of the small incidence PSPP geometry can be found in the Supporting Information. The disadvantage of this geometry is that the signal enhancement is smaller (∼5) for small incidence than for the near-Brewster geometry (∼30−50). However, a factor of 5 represents a significant improvement over the transmission experiment in terms of signal-to-noise ratio, making it feasible to acquire high-quality lifetime data on thin films.

2.4. Thin-Film Preparation. The SCN-based perovskite films were spin-coated onto SiO_2-coated (100 nm) CaF_2 substrates in a nitrogen glovebox. The CsBr (30 mg) or CsI (37 mg) and $Pb(SCN)_2$ (23 mg) at a molar ratio of 2:1 were dissolved in 450 μL of a 1:1 *N*,*N*′-dimethylformamide and dimethyl sulfoxide solvent mixture. Mild stirring and heating (80 °C) were necessary to dissolve CsBr completely. The solutions were filtered before spin coating. The precursor solution (100 μL) was dripped onto the substrate, and the substrate was spun at 3000 rpm for 60 s. The as-casted films were then annealed on a hot plate at 80 °C for 10 min. The film thickness was determined to be ∼70 nm by stylus profilometry (Figure S1). The phase purity of the films was assessed by powder X-ray diffraction (PXRD) (Figure S2).

3. RESULTS AND DISCUSSION

3.1. Absorption Spectra. As discussed above, the experiments were conducted on the CN stretch of SCN^- anions. To eliminate vibrational coupling and excitation transfer among SCN^- anions, the experiments were performed on ^{12}CN, with the sample isotopically diluted with the ratio of ^{13}CN to ^{12}CN ∼99%:1%. Figure 2 displays the FT-IR spectra of both the Br^-- (blue) and I^- (red)-containing samples. The large peaks in the main part of the spectra are from the high-concentration ^{13}CN stretches. Both the Br^- and I^- spectra are split into two bands. The peaks of the Br^- bands are located at 2037 and 2046 cm^{-1}. Their FWHMs are the same within error,

https://doi.org/10.1021/acs.jpcc.2c03516
J. Phys. Chem. C 2022, 126, 10145−10158

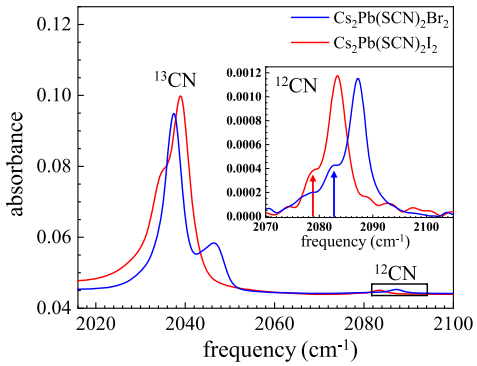

Figure 2. Main figure. FT-IR absorption spectra of the CN stretching mode of $Cs_2Pb(SCN)_2Br_2$ and $Cs_2Pb(SCN)_2I_2$ films at room temperature. The SCN groups in the films are ~99% ^{13}C. The splittings of the peaks are caused by coupling between nearby SCN^- anions. Inset: Expanded view of the 1% ^{12}CN absorption bands (baselined). In addition to the main peaks, there are ~30% amplitude side peaks (marked with arrows). The side peaks are not caused by resonant pair couplings as the concentrations are too low. The experiments were performed on the main bands of the low-concentration ^{12}CN stretches.

~5.7 cm^{-1}. The peaks of the I^- bands are located at 2035 and 2039 cm^{-1}. Their FWHMs are the same within error, ~4.8 cm^{-1}.

The same type of splitting was observed for $(MA)_2Pb(SCN)_2I_2$.[34] In that study, 2D IR spectroscopy showed that the ^{12}CN and ^{13}CN species were coupled. The 2D IR spectrum showed bands for both species and time-dependent oscillations in the spectra with frequency corresponding to the splitting between the ^{12}CN and ^{13}CN peaks in the linear absorption spectrum. This experiment definitely demonstrates coupling between CN moieties, but it does not tell which CNs are coupled. It was proposed that a pair of CN groups that reside in different 2D planes were coupled by transition dipole−transition dipole coupling. This interplane pair has the smallest separation between CNs in the lattice. The crystal structure of $(MA)_2Pb(SCN)_2I_2$[16,17,42,43] is depicted in Figure 1B.

For the two perovskites studied here, we also ascribe the splitting in the spectra to the coupling between the stretching modes of neighboring CN groups but not via the mechanism proposed previously. The peak splittings are ~9 and ~4 cm^{-1} for the Br^-- and I^--containing samples, respectively. We obtained the crystal structure of $Cs_2Pb(SCN)_2Br_2$ at 296 K (Figure 1C) to directly explore the interactions between CNs because most of our measurements, including the FT-IR spectra, were performed at room temperature. The room-temperature crystal structure has the same space group as the reported structure at 100 K but with slightly increased unit-cell parameters.[33] As shown in Figure 1C, the Br^- perovskite crystal has two adjacent SCN^- anions in different layers like in $(MA)_2Pb(SCN)_2I_2$. The two SCN^-s in the Br^- perovskite are perfectly antiparallel, while in $(MA)_2Pb(SCN)_2I_2$, they form an angle of 162°.

Although the distance between the SCN pairs in adjacent planes, ~4 Å, would produce a splitting into two CN vibrational states with frequency separations that are approximately as observed here and in $(MA)_2Pb(SCN)_2I_2$, the coupling between the CN pairs cannot be the correct explanation for the observed two CN spectroscopic bands for any of these perovskites. As the CN stretches are degenerate in the absence of coupling, the two vibrational eigenkets of the coupled pair will be the sum and difference of the CN local modes. Because the crystal structure of $Cs_2Pb(SCN)_2Br_2$ shows that the SCN^-s in the adjacent planes are exactly antiparallel, the transition dipoles of the two eigenstates will be the sum and difference of the local mode transition dipoles. The transition dipole of the eigenstate that is the difference of the local mode transition dipoles will have twice the local mode transition dipole because they are antiparallel, but the eigenstate that is the sum of the local modes will have zero transition dipole. Thus, one of the two eigenstates is dark and will not produce an absorption band. In $(MA)_2Pb(SCN)_2I_2$, the angle between the interplane pair of SCN^- is 162°. While not exactly parallel, so both states will have nonzero transition dipoles, the ratio of the peak intensities would be 36/1, again producing only one observable peak in the spectrum.

There are also translationally related SCN^-s in the unit cells of the same planes. These are separated by 6 Å in $Cs_2Pb(SCN)_2Br_2$. The transition dipole−transition dipole coupling falls off as $1/r^3$, so this coupling is quite weak. In addition, the translational symmetry will give rise to a vibrational exciton band (vibrational phonon, frequently called a vibron), not a pair splitting. The band shape and position would depend on the 2D exciton transition dipole−transition dipole coupling dispersion relation and the vibrational exciton−phonon coupling. The interplane pair coupling would produce two exciton bands, one of which would be dark.

A possible explanation for the pair splitting (two vibrational peaks) is suggested by the insets in Figure 1B,C. The crystal structure of $Cs_2Pb(SCN)_2Br_2$ shows that in a unit cell, there are two SCN^-s coordinated with a Pb^{2+}, which have a substantial angle of 34° between the two CN transition dipoles. The two CNs are separated by ~7 Å. The crystal structure of $(MA)_2Pb(SCN)_2I_2$ shows that the CNs have an angle of 43° and are ~7.5 Å apart. Although the crystal structure of $Cs_2Pb(SCN)_2I_2$ is not known, it is likely that the angle and the CN separations are approximately the same as that of $Cs_2Pb(SCN)_2Br_2$. In these compounds, transition dipole−transition dipole coupling would be too weak to account for the observed splitting. However, lead and sulfur have similar electronegativities. It is possible that there is a degree of covalent coupling between the two SCN^-s and the Pb^{2+}. Covalent bonding could give rise to coupling between the two nonparallel local CN modes, resulting in two normal modes, each with a significant transition dipole.

In addition to the possibility of splitting through covalent coupling, there should also be the vibrational exciton band associated with the coupling among the translationally equivalent SCN^-s. The amplitudes of the two peaks shown in the main portion of the spectrum in Figure 2 are very different for the Br^-- and I^--containing samples. For each type of perovskite, the relative amplitudes of the peaks vary from sample to sample. This was also observed for $(MA)_2Pb(SCN)_2I_2$ studied previously.[34] There may be three overlapping or more bands with different transition dipole directions. These types of perovskite films grow on a substrate with the crystallographic *a*-axis (layer stacking direction), on average, normal to the plane of the substrate.[17] We see strong preferential orientation for films of the Br^- perovskite with only (*h*00) reflections visible in the PXRD data; the I^- perovskite shows weaker orientation (Figure S3). In both cases, local variations in film thickness could result in the *a*-axis being tilted from the normal. The extent of the tilt could vary from one sample to another. The relative magnitudes of the

https://doi.org/10.1021/acs.jpcc.2c03516
J. Phys. Chem. C 2022, 126, 10145−10158

peaks would then vary because the projection of the *E*-field of the FT-IR beam onto the multiple transitions, producing overlapping bands, would vary because the transition dipoles do not point in the same directions. The complexity of the high-concentration spectrum through resonant coupling among different CNs and possible vibrational excitation transport is the reason that dilute ^{12}CNs were investigated.

In the main portion of Figure 2, in addition to the large peaks, there are low-amplitude bands in the range around 2086 cm^{-1}. These peaks are magnified in the inset. They arise from the 1% S^{12}CN$^-$ in each type of sample. The bands are the ^{12}CN absorptions in Br$^-$- (blue) and I$^-$ (red)-containing samples. Because the S^{12}CN$^-$s are in low concentration, the CNs do not have resonant interactions with other nearby CNs. Therefore, they do not have splittings caused by resonant interactions. The main peaks in the inset spectrum are located at 2087.2 cm^{-1} (Br$^-$, blue) and 2083.4 cm^{-1} (I$^-$, red).

There are at least two possible explanations for the small red shift of the CN stretch in the I$^-$- versus Br$^-$-containing sample. In a study of the perovskites MAPb(I/Br/Cl)$_3$, shifts of the methylammonium vibrational frequencies to lower frequency were ascribed to higher polarizability as the size of the halide increased.[44] The red shift of the CN band in the I$^-$-containing sample may also be caused by the higher polarizability of the I$^-$ film compared to the Br$^-$ film. Alternatively, since iodide is less electronegative than bromide, we expect less π donation from the SCN ligand to the metal in the I$^-$ film and more delocalization of the S lone pair over the SCN group, resulting in a slight weakening of the CN bond.

The FWHM of the CN stretch in both the Br$^-$- and I$^-$-containing samples is 4 cm^{-1}. In addition, each main peak has a small side peak shifted to lower frequency by 4.8 cm^{-1}. From sample to sample, these side peaks have the same frequencies, but their amplitudes relative to the corresponding main peaks appear to vary to some extent. The other small bumps in the spectra are baseline noise, which arise because of the very small absorptions of the samples. The side peaks are only a few tenths of an mOD. The baseline noise, which varies between samples, is likely responsible for the apparent change in the side peak amplitudes. These side peaks are obscured in the ^{13}CN spectra shown in the main portion of Figure 2 because of their low amplitudes, the splittings of the large peaks, and the wide wings of the main peaks to low frequency.

To understand the origin of the side peak, it is important to note that it is generated by the SCN$^-$ moiety. We first eliminated the possibilities of decomposition products, such as Cs(SCN) and Pb(SCN)$_2$, by FT-IR (see Figures S4 and S5). As discussed below in Section 3.2, Lifetime Measurements, we have measured the vibrational lifetimes of the main ^{12}CN peaks and the side peaks. The lifetime decay data of the side peak for the Br$^-$-containing sample is only ∼10% different from that of the main peak (see Figure 5). Lifetimes are sensitive to the chemical species. If the side peak was the result of a different moiety, it would not have a lifetime that is so similar to the main peak. Therefore the side peak can be assigned to S^{12}CN$^-$.

Figure 3 shows temperature-dependent spectra of the I$^-$-containing sample. The amplitudes of the main peaks have been matched. The side peak shows significant temperature dependence, becoming larger as the temperature is increased. A plot of the log of the amplitude of the side peak versus $1/T$ is shown in the inset, where T is the absolute temperature. As can be seen in Figure 3, the side peak absorbance is very small, particularly, at low temperature, and the baseline is not flat.

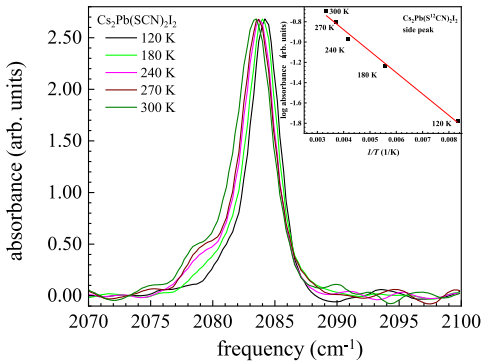

Figure 3. Temperature-dependent spectra of $Cs_2Pb(S^{12}CN)_2I_2$. The corresponding spectra for the Br$^-$-containing perovskite look very similar. The amplitudes of the main peaks have been matched at each temperature. The temperature dependence of the side peak can be clearly seen. Inset: The temperature-dependent amplitude of the $Cs_2Pb(S^{12}CN)_2I_2$ side peak plotted as the log of the absorbance vs $1/T$. The data points are fitted to a straight line, indicating an activated process with an activation energy of ∼160 cm^{-1}.

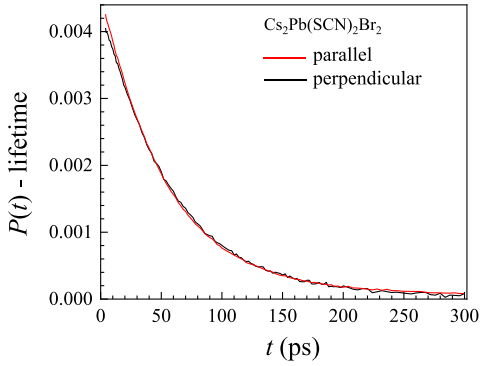

Figure 4. Pump−probe experimental decay data for $Cs_2Pb(S^{12}CN)_2Br_2$ with the probe parallel and perpendicular polarizations relative to the pump. The fact that the decays are essentially identical shows that there is no orientational motion during the times of the experiments. Therefore, the decay constants are the vibrational lifetime.

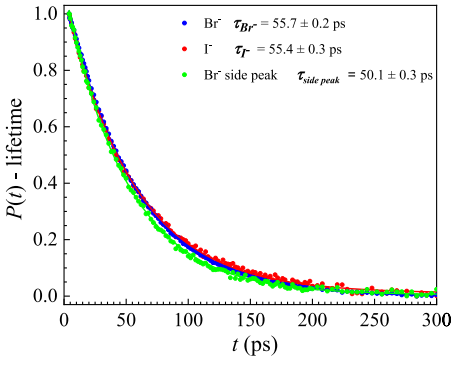

Figure 5. CN stretch vibrational population decays (lifetimes) for $Cs_2Pb(S^{12}CN)_2Br_2$ (blue) and $Cs_2Pb(S^{12}CN)_2I_2$ (red) films, side peak of $Cs_2Pb(S^{12}CN)_2Br_2$ (green), data (points), and single exponential fits (solid curves). The main peak lifetimes are identical within the very small experimental error. The side peak lifetime is very similar to that of the main peak, demonstrating that the side peak arises from the S^{12}CN$^-$ moiety.

Nonetheless, the data points fit well to a straight line, showing that they arise from an activated process. The activation energy

https://doi.org/10.1021/acs.jpcc.2c03516
J. Phys. Chem. C 2022, 126, 10145−10158

is ~160 cm^{-1}, but this number should be considered semiquantitative, given the weak absorption and the baseline noise. Temperature-dependent spectra for the Br^--containing sample look very similar.

Given the results presented in Figures 3 and 5, a reasonable explanation for the side peak is that there are SCN^- sites with two distinct conformations in the lattice resulting from two potential wells. The main peak arises from SCN^-s that occupy the lower energy well, and the side peak arises from SCN^-s that occupy the higher energy well. As the temperature increases, the occupation shifts toward the high energy well. Only one conformation is observed in the crystal structure. However, if the barrier between the wells is relatively low, rapid exchange, for example, within nanoseconds, between the conformations would likely be seen in the X-ray data as the average configuration. Furthermore, the perovskite films are deposited within minutes through spin coating, whereas the single crystals form in solution over a few days. The faster deposition of films can kinetically trap metastable intermediates not seen in the single-crystal structure. The difference in the conformation between the main ^{12}CN peak and the side peak is likely responsible for the small (10%) difference in the lifetime.

Although we assign all peaks in the IR spectrum related to the SCN groups, it is important to note that the experiments presented below were conducted on the main ^{12}CN bands of the Br^--and I^--containing samples. There are no contributions from the side peaks, and the concentration is too low for resonant $^{12}CN-^{12}CN$ interactions.

3.2. Lifetime Measurements. To determine the vibrational lifetimes of the CN stretch of the SCN^- anions in the Br^-- and I^--containing samples, we performed PSPP measurements in the small-incidence-angle geometry, as described above. The pump pulse was spectrally filtered with a Hann window by the AOM pulse shaper to avoid exciting the ^{13}CN stretch band. Essentially, the portion of the IR pulse spectrum that overlaps with the strong ^{13}CN absorptions was removed from the pulse spectrum. The elimination of strong absorption also eliminated the vast majority of sample heating.[34] Therefore, it was possible to obtain accurate vibrational relaxation dynamics of the ^{12}CN bands of the two types of films.

In a pump−probe experiment, the pump excites vibrations from 0 to 1 vibration levels. The excitation to the 1 level increases the transmission of the probe by partially bleaching the ground state (more probe transmission) and giving rise to stimulated emission (amplification of the probe). The initially excited vibrations tend to have their transition dipoles aligned with the electric field (*E*-field) direction of the pump. The probability amplitude of exciting a vibration is determined by the dot product of the *E*-field direction and the transition dipole direction, which is along the CN bond. The probability depends on the angle, θ, between the *E*-field and the CN bond (transition dipole direction) as $\cos^2\theta$. The initial signal will be larger for the probe polarization parallel to the pump pulse than perpendicular. The signal (increased probe transmission) will decay as molecules relax from the excited vibrational state to the ground state. Orientational relaxation, that is, rotation of the SCN^-, will also give rise to the time dependence of the signal, with the probe parallel signal decaying faster than the lifetime and the probe perpendicular signal decaying slower than the vibrational lifetime. As discussed in detail in Section 3.3, there is only a small amount of orientational relaxation, and it is so fast, ~100 fs, that it does not influence the pump−probe parallel and perpendicular measurements on the time scale of the experiments. Therefore, the parallel and perpendicular signal decays should be the same except for a multiplicative constant, and the decay time is the vibrational lifetime (population relaxation).

Figure 4 shows the pump−probe experimental decays for the Br^--containing samples. The perpendicular curve has been scaled, so its amplitude matches the parallel curve. Measurements were made on three samples. The results for the I^--containing samples are analogous. The parallel and perpendicular data are the same within experimental error. These results demonstrate that the decays do not have an orientational relaxation component and are governed strictly by the vibrational lifetime.

Figure 5 shows the lifetime decays for the Br^-- and I^--containing samples, as discussed above. The data are the points and single exponential fits are the solid curves for both types of films. The fits yield vibrational lifetimes of 55.7 ± 0.2 and 55.4 ± 0.3 ps for Br^-- and I^--containing samples, respectively. The lifetimes are identical within experimental error. The long vibrational lifetimes provide a considerable time window for monitoring fast structural changes in the perovskite lattice with 2D IR, as discussed below. Figure 5 also shows the lifetime decay of the side peak for the Br^--containing species. Its lifetime is 50.1 ± 0.3 ps.

Vibrational relaxation occurs because the excited vibration, the ^{12}CN stretch under study, is coupled to other modes in the system, that is, vibrations and phonons. The majority of the SCN^-, 99%, contains ^{13}CN. The ^{13}CN stretches on different anions will be weakly coupled via transition dipole−transition dipole interactions and can give rise to vibrational phonon bands (vibrons, i.e., vibrational excitons). However, the low-concentration ^{12}CN stretch is not resonant with the majority of ^{13}CN stretches. Therefore, the ^{12}CN stretch and the other vibrational modes of the $S^{12}CN^-$ are localized vibrations rather than delocalized vibrons. Because of the very weak interactions (narrow vibron bandwidth), even the ^{13}CN stretches are considered to be likely localized modes because of the inhomogeneous site energies and phonon-induced energy fluctuations (see Section 3.4 below).

Energy must be conserved. Therefore, relaxation of the ^{12}CN stretch must take place through a combination of vibrations and phonons that is equal to the initial excited-state energy.[45] In general, coupling via anharmonic terms in the potential to intramolecular modes, for example, SCN^-, is stronger than to intermolecular modes, for example, phonons and vibrons. The lowest order relaxation pathway, that is, the pathway involving the fewest modes, will be favored.[45] Because a combination of intramolecular modes is unlikely to exactly match the initial excited-state energy, ~2084 cm^{-1} for both the Br^-- and I^--containing samples, relaxation will occur by exciting several lower frequency vibrations of SCN^- and one or more phonons. SCN^- has three internal modes in addition to the CN stretch, the S−C stretch, and two degenerate SCN bends, which have frequencies of ~743 and ~470 cm^{-1}.[46,47] A likely relaxation pathway would be through the annihilation of the CN stretch, the creation of three S−C stretches for a total of ~2229 cm^{-1}, and the annihilation of a phonon to conserve energy. The CN stretch energy is ~2084 cm^{-1}. Room temperature is about 200 cm^{-1}. A thermally populated phonon of ~145 cm^{-1} would be annihilated. In addition to the coupling strengths of the initial vibration to the other modes,

https://doi.org/10.1021/acs.jpcc.2c03516
J. Phys. Chem. C 2022, 126, 10145−10158

the magnitude of the phonon density of states at 145 cm^{-1} will in part determine the rate of relaxation. Given the constituents of the lattice, it is reasonable to assume that there is a significant phonon density of states at 145 cm^{-1}. Another possible pathway would be the relaxation of the initially excited CN stretch by creating two S−C stretches and one bend, which equals 1956 cm^{-1}, and the creation of a 129 cm^{-1} phonon. Again, there is likely to be a significant phonon density of states at 129 cm^{-1}. Both of these processes are fifth order, and both may be involved in the relaxation. Since the first process requires a thermally populated phonon, a temperature-dependent study might be able to determine the contribution of the possible pathways.

The CN stretch lifetimes in the Br^- and I^- perovskites are essentially identical. As discussed immediately above, the vibrational relaxation pathway likely involves the creation of three SCN^- low-frequency modes and either the creation or the annihilation of a low-frequency phonon. The CN stretch frequencies in the two types of perovskites are virtually the same, which is a strong indication that the S−C stretch and bend frequencies of the two perovskites are also virtually identical. Therefore, the frequencies of the phonons involved in the relaxation will be almost the same as well. Creation or annihilation of a phonon depends on the coupling to the phonon and the density of states at the phonon frequency. Replacing Br^- with I^- will change the phonon spectrum, for example, reduce the Debye cutoff for the acoustic phonons. The fact that the Br^- and the I^- perovskites have the same vibrational lifetimes implies that the part of the phonon spectrum that is coupled to the CN stretch is unaffected by the change in mass of the halide anion.

The lifetimes measured here are considerably longer than the CN stretch lifetime in $(MA)_2Pb(SCN)_2I_2$, which is 11.6 ± 0.1 ps. The most significant difference is the high-frequency modes of the ammonium cation. These will give rise to narrow vibrational exciton bands that have approximately the frequencies of the ammonium vibrational modes. To determine if the ammonium vibrational modes contribute to the substantially shorter lifetime in $(MA)_2Pb(SCN)_2I_2$ versus the two inorganic perovskites studied here, the CN lifetime in the deuterated variant $(MA\text{-}d_6)_2Pb(SCN)_2I_2$ was measured in the same manner as the other lifetimes. The CN stretch in $(MA\text{-}d_6)_2Pb(SCN)_2I_2$ has a lifetime of 7.4 ± 0.1 ps, which is considerably shorter than in $(MA)_2Pb(SCN)_2I_2$ (Figure S8). As the deuteration will not change the lattice structure and leaves the phonon spectrum almost unchanged, the difference in lifetime must arise from the substantial differences in the vibrations of $(MA)_2Pb(SCN)_2I_2$ versus $(MA\text{-}d_6)_2Pb(SCN)_2I_2$, demonstrating the importance of the ammonium vibrational modes in the fast CN vibrational relaxation of $(MA)_2Pb(SCN)_2I_2$.

We can only speculate on why $(MA)_2Pb(SCN)_2I_2$ has faster CN vibrational relaxation than the Br^-/I^- systems, but there are some qualitative considerations that are intriguing. The N−H stretches are ∼3050 cm^{-1}, and the C−H stretches are ∼2950 cm^{-1}. These are unlikely to participate in the vibrational relaxation of the CN stretch at ∼2084 cm^{-1}. Annihilation of the CN mode and creation of an N−H or C−H stretch would require the annihilation of a phonon in the 900−1000 cm^{-1} range, which would have a very low probability of thermal excitation and probably does not exist in the phonon spectrum. Energy could be conserved by annihilating several lower frequency phonons, but this would lead to an unfavorable high-order process. However, there are two bends at 1418 and 1536 cm^{-1} in MA.[48] Annihilation of the CN stretch, creation of the S−C stretch (743 cm^{-1}), creation of one of the MA bends, and annihilation of a phonon (∼100 cm^{-1}) would result in fourth-order processes. The proposed mechanisms for relaxation of the CN stretch in the Br^-/I^- systems are both fifth order. The lower order of the process in $(MA)_2Pb(SCN)_2I_2$ would probably result in faster relaxation.[45]

The even faster relaxation of the CN stretch in the MA-d_6 perovskite could be a result of the lower frequency vibrational modes of the deuterated methylammonium. For example, MA-d_6 has a C-D stretch at 2129 cm^{-1}.[49] Annihilation of the CN stretch, excitation of this C−D stretch, and the annihilation of a 45 cm^{-1} phonon would be a third-order process. Alternatively, there is an MA-d_6 N−D stretch at 2282 cm^{-1} requiring the creation of a 198 cm^{-1} phonon, which would also be a third-order process. Both of these phonons are thermally populated at room temperature. All of the N−D and C−D stretches have similar frequencies. Therefore, there are a large number of third-order pathways that will be involved to an extent determined by the coupling constant, the phonon density of states, and the thermal phonon occupation number for each pathway.[45] These third-order pathways will likely result in faster vibrational relaxation than the fourth-order process discussed above for the protonated MA perovskite.

3.3. Anisotropy Measurements. When a probe ion or molecule, for example, $SeCN^-$, is placed in a liquid, orientational relaxation will occur as a result of orientational diffusion.[50] In a liquid, a probe molecule will sample all orientations on some time scale. In an isotropic 3D system (transition dipoles point randomly in all directions), the parallel and perpendicular signals are related to the population relaxation $P(t)$ and the second-order Legendre polynomial orientational correlation function $C_2(t)$ by

$$I_{\parallel} = [1 + 0.8C_2(t)] \times P(t)$$
$$I_{\perp} = [1 - 0.4C_2(t)] \times P(t) \quad (2)$$

Then, the population relaxation (exponential lifetime decay) is given by

$$P(t) = [I_{\parallel}(t) + 2I_{\perp}(t)]/3 \quad (3)$$

and the time-dependent orientational anisotropy (orientational relaxation) is[51,52]

$$r(t) = \frac{I_{\parallel}(t) - I_{\perp}(t)}{I_{\parallel}(t) + 2I_{\perp}(t)} = 0.4C_2(t) \quad (4)$$

Equation 4 relates PSPP experiments to the orientational dynamics obtained by measuring the polarization components of the probe pulse parallel and perpendicular to the pump pulse. The data give $r(t)$, the anisotropy. For an isotropic system, multiplying $r(t)$ by 2.5 (eq 4) yields the second Legendre polynomial orientational correlation function, $C_2(t)$. The polarized pump pulse excites an anisotropic distribution of molecules into the first vibrational excited state determined by the dot product of the E-field direction and the direction of the vibration's transition dipole quantity squared. The initial distribution of excited transition dipoles is cosine-squared. The distribution looks like a 2p orbital probability distribution. This results in more probe signal when the probe polarization is parallel to the pump polarization (∥) than when it is perpendicular (⊥). In a liquid, eventually, all molecules

https://doi.org/10.1021/acs.jpcc.2c03516
J. Phys. Chem. C 2022, 126, 10145−10158

randomize their directions, and $I_{\parallel}$ and $I_{\perp}$ become identical if the vibrational lifetime is sufficiently long to see the complete orientational randomization of the probe molecules. The signal decays to zero.

However, even for the case of molecules in a simple liquid, $r(t)$ is not observed to begin at 0.4, the maximum value of the anisotropy (see eq 4). There are extremely fast (tens of femtoseconds) inertial motions that are generally too fast to measure their decay constant. However, the amplitude of the inertial decay can be determined by extrapolating the measured decay curve, which begins somewhat after $t = 0$, back to $t = 0$.

For the perovskites studied here, the CN transition dipoles are not randomly distributed in a single crystal. Spin coating results in thousands of crystallites within the laser beam. These crystallites have their surface planes essentially parallel to the plane of the substrate but have random orientations in the plane.[17] The SCN^- makes a 17° angle with the plane (CN transition dipole direction).[33] Hence, the isotropic 3D model cannot properly describe orientational motions of SCN^-s. Instead, as shown in previous publications,[53,54] the observed parallel and perpendicular signals are given by

$$I_{\parallel} = \left[1 - 2\langle S\rangle + C^{op}(t) + \frac{9}{8}C^{mip}(t)\right] \times P(t)$$

$$I_{\perp} = \left[1 - 2\langle S\rangle + C^{op}(t) - \frac{9}{8}C^{mip}(t)\right] \times P(t) \quad (5)$$

where $\langle S\rangle$ is the order parameter, $C^{op}(t)$ and $C^{mip}(t)$ are the out-of-plane and mainly in-plane components of the orientational correlation functions, respectively. The orientational motions of SCN^-s in their lattice sites are highly restricted. Complete orientational relaxation will not occur. However, ultrafast librational motions can occur. The observed anisotropy can convey information about the librational motions of the SCN^-s.

As discussed above, the experiments were conducted on ^{12}CN at 1% concentration to eliminate vibrational excitation transfer between identical CNs. At this concentration, nearby SCN^- anions will contain ^{13}CN, which is not resonant with the ^{12}CN. Therefore, vibrational excitation transfer will not produce orientational relaxation by transferring the excitation between SCN^- with transition dipoles pointing in different directions. The blue curve in Figure 6A shows anisotropy data for the Br^--containing sample at 1% ^{12}CN concentration. As anticipated, within the signal-to-noise ratio, the anisotropy, $r(t)$, is time independent, demonstrating that there is no diffusive orientational relaxation, in contrast to a liquid. The data show the same lack of orientational relaxation for the I^--containing sample.

Wobbling-in-a-cone theory applies when the complete orientational relaxation cannot occur,[55−57] and it can be utilized to evaluate the inertial motions of the SCN^-s, which are quantified by the cone angle, in this case, the angular range that the SCN^- samples as it undergoes librational motion. The modified wobbling-in-a-cone theory has been developed for uniaxial systems, which is referred to as the tilted cone model.[53,54] Figure 6B shows an illustration of the tilted cone model. Since our experimental time window begins after and is much longer than the time scale of the inertial motions, we can evaluate $\langle S\rangle$, $C^{op}(t)$, and $C^{mip}(t)$ in the infinite time limit. (The full time-dependent equations have been presented.[53,54]) The infinite time equations are given by

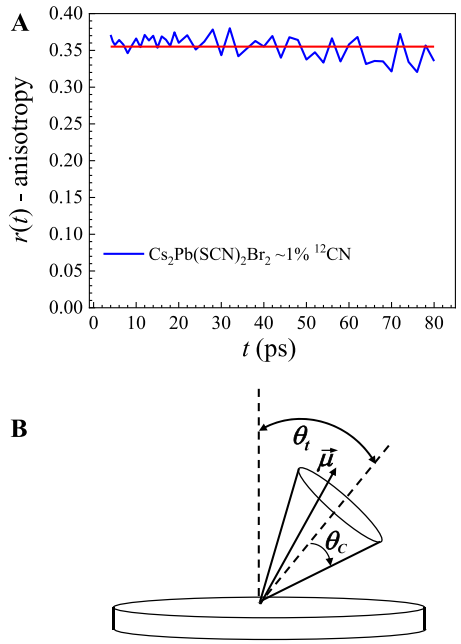

Figure 6. (A) Anisotropy decay of the $S^{12}CN^-$ anions of $Cs_2Pb(S^{12}CN)_2Br_2$. The decay for the I^- perovskite is similar. The data are horizontal within experimental error, demonstrating that after ultrafast librational motions, there is no further orientational relaxation. (B) Schematic of the wobbling-in-a-tilted-cone model. The cone axis is tilted by θ_t from the planar surface normal. The wobbling (librational) cone half angle is θ_C.

$$\langle S\rangle = \frac{3\cos^2\theta_t - 1}{4}\cos\theta_C(1 + \cos\theta_C) \quad (6)$$

$$C^{op}(t) = \frac{(3\cos^2\theta_t - 1)^2}{16}[\cos\theta_C(1 + \cos\theta_C)]^2 \quad (7)$$

$$C^{mip}(t) = \frac{\sin^4\theta_t}{4}[\cos\theta_C(1 + \cos\theta_C)]^2 \quad (8)$$

where θ_t is the tilt angle and θ_C is the cone half angle, that is, the half angle of the librational motion. θ_t is the tilt angle from the normal to the plane. From the crystal structure, θ_t is 73°. Using eqs 6−8 in eq 5 and substituting these into eq 4 give the expression for $r(t)$. The result is an equation that describes the observed anisotropy data in Figure 6B when consideration of the pump−probe crossing angle is included (see the Supporting Information). There is only one adjustable parameter, θ_C, which was determined to be 13 ± 2° for the Br^--containing sample. Although we do not have the single-crystal structure of the I^--containing sample, given the similarities in measurements on the two perovskites presented in this paper, we will assume that their SCN^- tilt angles are very similar. If θ_t is also 73° in the I^--containing sample, its θ_C is found to be 16 ± 2°. We found that a variance of 2° in the tilt angle only changes the cone angle by ~0.1°. Within the error of the measurements, the librational cone angles are the same for the two perovskites.

3.4. 2D IR Spectral Diffusion Measurements. The 2D IR experiments measure spectral diffusion and the homogeneous contribution to the absorption line shape. The frequency of a CN stretch is in part determined by its environment. Intermolecular interactions shift the vibrational frequency. If the vibrations of an ensemble of molecules experience different

https://doi.org/10.1021/acs.jpcc.2c03516
J. Phys. Chem. C 2022, 126, 10145−10158

intermolecular interactions, there will be a range of vibrational frequencies, that is, inhomogeneous broadening. In the perovskites, if the environments of the SCN^-s are continually interconverting among the range of frequencies in the inhomogeneously broadened spectrum, their frequencies will fluctuate. This frequency evolution is spectral diffusion. Spectral diffusion is caused by structural fluctuations. Therefore, measuring the temporal dependence of spectral diffusion is measuring the time-dependent perovskite lattice structural fluctuations.

The CN moiety has a large and well-characterized first-order Stark coupling.[58−61] Therefore, a possible source of spectral diffusion in the perovskites is structural changes in the environments of the SCN^- anions that give rise to changes in the electric field along the CN bond. A component of the structural fluctuations that is very fast compared to the range of frequencies sampled ($\Delta\tau \ll 1$, see eq 1) results in motional narrowing and produces a homogeneous contribution to the absorption line shape. The homogeneous contribution is not T_w-dependent, so it does not contribute to the CLS(T_w) and is not part of the measured spectral diffusion.

Figure 7 shows 2D IR spectra of the Br^- (top) and I^- (bottom) perovskites at two T_ws, 4 and 80 ps. Given the

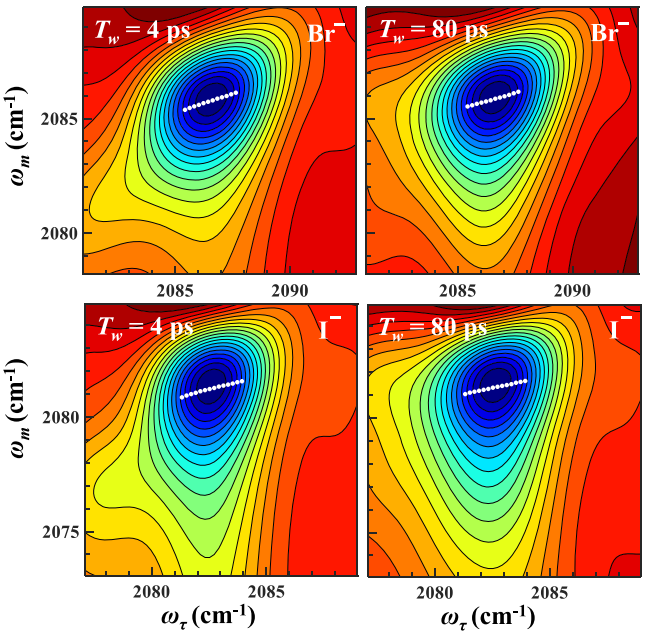

Figure 7. 2D IR spectra of the CN stretch of the $Cs_2Pb(S^{12}CN)_2Br_2$ and $Cs_2Pb(S^{12}CN)_2I_2$ films at two times, T_w = 4 and 80 ps. The white dots define the center line. The change in the center line slope with T_w, CLS(T_w), gives the normalized frequency−frequency correlation function.

samples have absorbances of ∼1 mOD (0.001 absorbance), the signal quality is high because of the use of the near Brewster's angle reflection geometry.[40,41,62] The line of white dots in each spectrum defines the center line.[37] The change in slope of the center line with T_w, the CLS(T_w), gives the normalized FFCF. Although the observed changes in slope with time (T_w) are small, they are readily measured. From CLS(T_w) and the FWHM of the absorption line, the complete FFCF, including the homogeneous contribution, is determined.[37,38] The 2D IR spectra were acquired only from the ^{12}CN band by pumping with AOM pulse shaping to avoid CLS oscillation caused by the vibrational coupling between the ^{12}CN and ^{13}CN bands.[34] Because the I^--containing samples scatter substantially more than the Br^--containing samples, an eight shot phase cycling/chopping sequence was used to remove the scatter contribution from the 2D spectra,[63] and the ^{12}CN ratio was increased to 2% to enhance the signal-to-noise ratio. PSPP measurements confirmed that there was no excitation transfer after increasing the isotope ratio.

Figure 8 displays the CLS(T_w) decays for the Br^-- (top) and I^- (bottom)-containing samples. The data shown in Figure 8

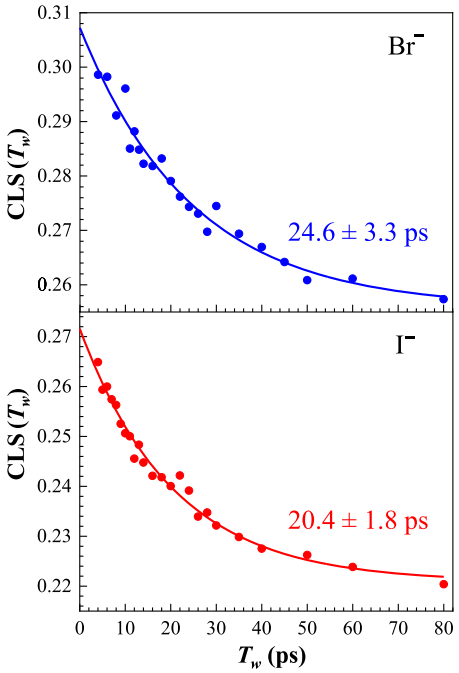

Figure 8. CLS(T_w) decays of the CN stretch of the $Cs_2Pb(S^{12}CN)_2Br_2$ (blue) and $Cs_2Pb(S^{12}CN)_2I_2$ (red) films. The dots are the data, and the solid curves are fitted to a single exponential decay with an offset. The difference between the T_w = 0 and 1 gives the homogeneous component of the line shape. CLS(T_w) decays show that there are inhomogeneous broadening and structural fluctuations sensed by the CN moiety. Within experimental error, the structural fluctuation-induced spectral diffusion is the same for the two perovskites. The offset indicates that there is also static inhomogeneous broadening from, for example, crystal lattice strains.

are the average of data from three independent samples. The decay curves were fit to a single exponential plus an offset. The offset reflects dynamics that are too slow to measure, given the experimental time window determined by the vibrational lifetime. Formally, the CLS(T_w), which is the normalized FFCF, begins at 1. Extrapolating the data back to T_w = 0, it is seen that the initial experimental values are well below 1. The difference between 1 and the experimental initial value of the CLS(T_w) is related to the homogeneous contribution to the absorption line shape and is used to obtain it. Given the experimental error in extrapolating the curves to T_w = 0, the two values are very close at 0.31 ± 0.12 and 0.27 ± 0.02 for the Br^-- and I^--containing samples, respectively. The CLS(T_w) decays are also the same within experimental error, that is, 24.6 ± 3.3 and 20.4 ± 1.8 ps for the Br^-- and I^--containing samples, respectively. The observed decay reflects a partial sampling of the inhomogeneous spectrum.

https://doi.org/10.1021/acs.jpcc.2c03516
J. Phys. Chem. C 2022, 126, 10145−10158

Even after 80 ps, which is the probe vibrational lifetime limited time window of the measurement, the CLS(T_w) is significantly above 0. This demonstrates that there is structural inhomogeneity that is not sampled within 80 ps. One possibility for the additional inhomogeneity is that there is a static component to the inhomogeneous broadening. A static component could be caused by, for example, crystal strains. Strains slightly change the local lattice parameters, which in turn change the CN frequencies by changing the interactions of the CNs with the surrounding ions. As mentioned above, CN is very sensitive to electric fields through the first-order Stark effect.[58−61] Strain-induced changes in ion positions will change the electric field along the CN axis, shifting the frequency. A range of strain amplitudes and directions in the crystallites that make up the films could result in static variations in CN frequencies, that is, static inhomogeneous broadening. The second possibility is that at least some of the long-time inhomogeneous broadening is dynamic, and in addition to the observed ∼20 ps decay, there is a much slower decay. Fits with a second decay of >20 ns are indistinguishable from the fits with a static offset. Therefore, we cannot determine the nature of the long-time behavior of the inhomogeneous broadening. However, the size of the offset used in the fits varied somewhat from sample to sample. This variation suggests that at least some of the offset is caused by strains and possible defects that arise from differences in the crystallites that occur in spin coating.

The absorption spectrum has homogeneous and inhomogeneous components. We used the CLS(T_w) decays and the FWHM of the absorption spectra to obtain the full FFCFs using a recently developed extension of the CLS method[37,38] that employs artificial neural networks.[64] Within experimental error, the results for the Br^- and I^- perovskites are the same. The homogeneous line width of both perovskites was found to be ∼2.8 cm^{-1}. The inhomogeneous width is 2 cm^{-1}, and the total line width is 4 cm^{-1}. Therefore, the homogeneous broadening is somewhat larger than the inhomogeneous broadening.

Homogeneous broadening comes from the direct coupling of the CN stretch frequency to phonons. Skinner and coworkers utilized a nonperturbative theoretical method to analyze vibrational line shapes from experimental data for both ionic crystals and molecular crystals.[65−67] The detailed results showed that the homogeneous broadening in crystals is through phonon modulation of the vibrational transition frequency. A single coherent phonon is a wave that can, for example, modulate the density of the crystal at the site of a vibration. A great number of thermally populated phonons will have a wide range of frequencies and relative phases. In the perovskites studied here, the samples are at room temperature, that is, k_BT = ∼200 cm^{-1}. Phonons from low frequency to frequencies greater than 200 cm^{-1} will be thermally populated. Without knowing the phonon dispersions and the phonon−vibration (vibron) coupling, we cannot say which types and frequencies of phonons are responsible for homogeneous dephasing. However, it seems clear that there will be very rapid modulations of the ensemble of CN vibrational frequencies, which will result in motional narrowing and, therefore, homogeneous dephasing. Temperature-dependent 2D IR measurements of the homogeneous line widths could shed light on the mechanism that gives the homogeneous line width.

While homogeneous dephasing arises from the direct coupling of phonons to the CN stretch, spectral diffusion is different. The phonon motions cause the vibrational frequencies to fluctuate. Spectral diffusion is caused by time-dependent structural changes in the surrounding lattice environment of SCN^-s. At a given time, different CNs are experiencing different lattice environments producing different CN frequencies. As discussed above, some of the distinct lattice environments are static or very long-lived. Others are dynamic on a relatively short time scale and can be driven to change through coupling to the thermal bath (phonons). Figure 9 shows a heuristic illustration of the spectral diffusion.

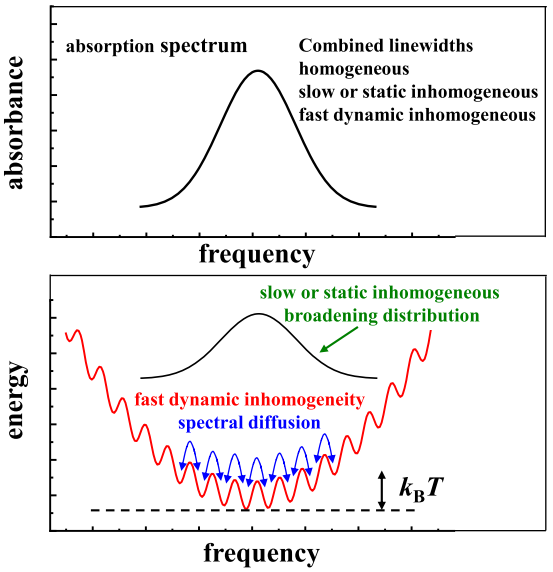

Figure 9. Schematic illustration of the inhomogeneous contributions to the lineshape. Structural dynamics that give rise to spectral diffusion are indicated by the blue curved arrows representing transitions among transitory structural configurations on the energy landscape. Changes in the CN's environment cause changes in intermolecular interactions that result in the frequency of the CN stretch to fluctuate. The convolution of the dynamic and static inhomogeneous broadening comprises the inhomogeneous portion of the CN absorption spectrum. The homogeneous broadening is an additional contribution to the line shape.

The CNs experience a range of environments, which result in different intermolecular interactions and, therefore, different vibrational frequencies. Then, for a short time, the CNs reside in environments that are at local energy minima, illustrated in Figure 9. Thermal fluctuations can cause an environmental change, resulting in transitions from one local minimum to another on the energy landscape (curved arrows in Figure 9). In the diagram, the minima are all of the same depth. In the lattices, there will be a range of depths. The structural evolution results in the CN frequency evolution, which is spectral diffusion. The 2D IR experiment is carried out to measure the time dependence of the spectral diffusion and, therefore, the time dependence of the structural changes that cause the CN frequency to change.

The fact that the Br^- and I^- perovskites have the same spectral diffusion dynamics within experimental error means that their energy landscapes are the same or very similar. The absorption line shapes are essentially identical (see Figure 2 inset). The absorption line shape is determined by homogeneous and inhomogeneous contributions. The 2D IR experiments show that both of these contributions are the same for the Br^- and I^- perovskites. In addition, the CN

https://doi.org/10.1021/acs.jpcc.2c03516
J. Phys. Chem. C 2022, 126, 10145−10158

vibrational lifetimes are the same in the two types of perovskites. Therefore, the change from one halide to the other in these two perovskites does not change the lattice structural dynamics or the range of inhomogeneous energies reported by the CN vibration. It is important to emphasize that lattice structural dynamics, manifested as spectral diffusion, homogeneous broadening, or static inhomogeneous broadening that do not couple to the CN frequency will not be observed in these experiments.

It is not known what is responsible for the observed dynamic spectral diffusion, that is, dynamic inhomogeneity. The following speculations on possible mechanisms for spectral diffusion are only intended to indicate why the 2D crystal lattice can be dynamic. One possibility is that there are dislocations in the lattice. The lattice structure is the same on either side of a dislocation, but the lattice structure is displaced by some amount. Movement of dislocations, known as glide or slip, occurs in lattices.[68] The 2D layered nature of the perovskites studied here and previously[34] may be amenable to dislocations and slip driven by phonons. The SCN^- environment, for example, electric fields, would be expected to be different near a dislocation than in other locations in a crystal. Dislocations could cause inhomogeneous broadening, and slip could result in time-dependent CN frequencies, that is, spectral diffusion.

Another possibility is a mechanism in which phonons drive the formation of shallow short-lived potential wells associated with a distorted structure. The perovskite is composed of 2D planes. Phonons will distort the planes both in plane and out of plane. At room temperature, the phonons are relatively localized propagating wave packets rather than fully delocalized waves. These wave packets will cause relatively local distortions of the lattice planes. It may be possible that phonon modulations of a 2D plane result in local distortions that lower the cohesive energy. The result would be relatively shallow potential wells that maintain the distortions for a short time after the phonons are no longer present. In some sense, this is like a molecular Jahn−Teller distortion, but here, thermal energy is required to drive a lattice distortion rather than having the intrinsic nature of the molecular orbitals drive the distortion. Distortion of the high-symmetry 2D plane results in lowering the energy. Shallow potential wells are created. There is enough thermal energy to activate the distorted structures out of the wells. A wide range of such distortions of the planes with a wide range of well depths might exist. These local transitory distortions change the environments of the SCN^- and therefore the CN frequencies. The shallow wells lead to fast spectral diffusion. Such distortions, although longer lived than phonon distortions, are transitory with short lifetimes. Therefore, like direct phonon-induced distortion, they would not show up in the X-ray structure. Such distortions have been observed in the photoexcited states of 2D lead-bromide perovskites through transient absorbance measurements and are associated with exciton self-trapping.[69] Here, it is suggested that the distortions occur in the absence of electronic excitation.

It is interesting to note that the spectral diffusion of the CN stretch of SCN^- in $(MA)_2Pb(SCN)_2I_2$ is ~4 ps compared to the ~20 ps for the two perovskites studied here.[34] As discussed in connection with the differences in the lifetimes of the CN stretch in $(MA)_2Pb(SCN)_2I_2$ compared to the Br^- and I^- perovskites, the presence of the MA group adds degrees of freedom, and orientational motions of the MA may contribute to the faster structural fluctuations. The absorption line width of the $(MA)_2Pb(SCN)_2I_2$ ^{12}CN stretch is ~7.5 cm^{-1} compared to ~4 cm^{-1} for the Cs perovskites. As the CN-reporting species are identical in the two types of perovskites, the broader line width in the MA perovskite indicates a wider range of structures. It is possible that these differences arise from the rotational freedom of the methyl and ammonium groups of $(MA)_2Pb(SCN)_2I_2$.

4. CONCLUDING REMARKS

Here, we have presented a detailed study of the lattice dynamics of two inorganic pseudohalide 2D perovskites, $Cs_2Pb(SCN)_2Br_2$ and $Cs_2Pb(SCN)_2I_2$. The 2D IR experiments (see Figures 7−9) showed that the absorption spectra are inhomogeneously broadened, and both perovskites undergo spectral diffusion of the CN stretch frequency. The observation of spectral diffusion demonstrates that not only there are distinct structural environments for different SCN^- anions but also these structures interconvert on a 20 ps time scale. Previously, 2D IR experiments showed that the 2D perovskite, $(MA)_2Pb(SCN)_2I_2$, also underwent spectral diffusion.[34] The perovskites studied here do not have an organic cation. Perhaps, the most important result from the current study is the direct observation of fast structural evolution (spectral diffusion) in all-inorganic 2D perovskites, which shows that structural dynamics do not require organic cations. A time-independent low-frequency Raman scattering study of the 3D $CsPbBr_3$ perovskite using line shape analysis indicated that intrinsic local polar fluctuations of the lead halide perovskite structure did not require dipolar organic cations.[26] The 2D perovskite study presented here allowed us to use a vibrational probe (SCN^-), which would disrupt the structure of a 3D perovskite. However, we can reasonably extend our conclusions about picosecond timescale lattice dynamics to 3D perovskites regardless of the A-site cation (organic or inorganic). The local and/or mesoscopic lattice structure varies with location, and the structural variations fluctuate on a picosecond timescale (see the schematic illustration in Figure 9). The observation of these structural fluctuations can have profound implications for the properties of the electronic excited states. The structural fluctuations can influence exciton transport and exciton self-trapping and may play an important role in the mechanism of "white" light emission from certain 2D perovskites.[70] An exciton or charged particle is not moving in a perfect lattice subject only to phonon scattering. These species are moving in imperfect inhomogeneous lattices and can be scattered, trapped, and detrapped by the time evolution of the environments they are moving through.

In addition to 2D IR experiments, the reflection geometry PSPP experiments were performed to determine the CN stretch vibrational lifetimes and the anisotropy dynamics (orientational dynamics) of the 2D perovskite thin films. The lifetimes of the Br^- and I^- perovskites were the same within experimental error (55 ps; see Figure 5). The fact that the lifetimes are the same shows that the CN vibration couples to the phonon bath independent of whether the halide anion is Br^- or I^-. Changing the halide will change the phonon dispersion to some extent but not in a manner that affects the CN stretch vibrational energy deposition into the phonon bath. Thus, from the perspective of the CN, the phonon density of states and the coupling of the high-frequency CN stretch to the phonon bath are unchanged.

https://doi.org/10.1021/acs.jpcc.2c03516
J. Phys. Chem. C 2022, 126, 10145−10158

Anisotropy measurements on the low-concentration (1%) $S^{12}CN^-$ anions' CN stretch showed an initial decay of the orientation of the SCN^-s caused by ultrafast librational motions. Within error, the extent of the decays for the two types of perovskites was the same. At a longer time, the anisotropy did not decay, which is expected as the SCN^- anions' orientations are fixed by the lattice except for the librational motions.

Future experiments will include detailed studies of the anisotropy of these and other 2D perovskites and measurements with a visible pump (~400 nm) to produce excitons followed by nonlinear IR experiments. Of particular importance will be 2D IR spectroscopy after visible pumping. By chopping the visible pump, we can obtain 2D IR data for the electronically excited states. These experiments have the potential to measure lattice structural dynamics and spectral diffusion in the electronic excited states, that is, in the presence of excitons.

■ ASSOCIATED CONTENT

Supporting Information

The Supporting Information is available free of charge at https://pubs.acs.org/doi/10.1021/acs.jpcc.2c03516.

Crystallographic data of $Cs_2Pb(SCN)_2Br_2$ (CIF)

Profilometry measurement of the $Cs_2Pb(SCN)_2Br_2$ film; room-temperature crystallographic data of $Cs_2Pb(SCN)_2Br_2$; PXRD of $Cs_2Pb(SCN)_2X_2$ films; FT-IR spectra of $Pb(SCN)_2$ and Cs(SCN); and small-incidence-angle reflection PSPP method population decay of the $(MA\text{-}d_6)_2Pb(SCN)_2I_2$ film (PDF)

■ AUTHOR INFORMATION

Corresponding Authors

Hemamala I. Karunadasa − *Department of Chemistry, Stanford University, Stanford, California 94305, United States; Stanford Institute for Materials and Energy Sciences, SLAC National Accelerator Laboratory, Menlo Park, California 94025, United States;* orcid.org/0000-0003-4949-8068; Phone: 650 723-0288; Email: hemamala@stanford.edu

Michael D. Fayer − *Department of Chemistry, Stanford University, Stanford, California 94305, United States;* orcid.org/0000-0002-0021-1815; Phone: 650 723-4446; Email: fayer@stanford.edu

Authors

Xiangyu Xing − *Department of Chemistry, Stanford University, Stanford, California 94305, United States*

Jiayi Li − *Department of Chemistry, Stanford University, Stanford, California 94305, United States*

John P. Breen − *Department of Chemistry, Stanford University, Stanford, California 94305, United States*

Jun Nishida − *Center for Mesoscopic Sciences, Institute for Molecular Science, Okazaki, Aichi 444-8585, Japan;* orcid.org/0000-0001-7834-8179

Complete contact information is available at: https://pubs.acs.org/10.1021/acs.jpcc.2c03516

Author Contributions

X.X., J.L., and J.P.B. contributed equally. J.N. did the analysis of the librational cone angle using the tilted cone theory. The manuscript was written through contributions of all authors.

Notes

The authors declare no competing financial interest.

■ ACKNOWLEDGMENTS

This work was supported by the Air Force Office of Scientific Research grant number FA9550-16-1-0104 (X.X., J.P.B., and M.D.F.). Work by J.L. and H.I.K. was funded by the National Science Foundation (DMR-1904443). J.L. is grateful for a Stanford Interdisciplinary Graduate Fellowship. Part of this work was performed at the Stanford Nano Shared Facilities (SNSF), supported by the National Science Foundation under award no. ECCS-2026822. We greatly appreciate Ching-Ting Tsai's help with fabricating several SiO_2-coated CaF_2 substrates.

■ REFERENCES

(1) Ishihara, T.; Takahashi, J.; Goto, T. Exciton State in Two-Dimensional Perovskite Semiconductor $(C_{10}H_{21}NH_3)_2PbI_4$. *Solid State Commun.* **1989**, *69*, 933−936.

(2) Smith, I. C.; Hoke, E. T.; Solis-Ibarra, D.; McGehee, M. D.; Karunadasa, H. I. A Layered Hybrid Perovskite Solar-Cell Absorber with Enhanced Moisture Stability. *Angew. Chem., Int. Ed.* **2014**, *53*, 11232−11235.

(3) Tsai, H.; Nie, W.; Blancon, J.-C.; Stoumpos, C. C.; Asadpour, R.; Harutyunyan, B.; Neukirch, A. J.; Verduzco, R.; Crochet, J. J.; Tretiak, S.; et al. High-Efficiency Two-Dimensional Ruddlesden−Popper Perovskite Solar Cells. *Nature* **2016**, *536*, 312−316.

(4) Tsai, H.; Asadpour, R.; Blancon, J.-C.; Stoumpos, C. C.; Even, J.; Ajayan, P. M.; Kanatzidis, M. G.; Alam, M. A.; Mohite, A. D.; Nie, W. Design Principles for Electronic Charge Transport in Solution-Processed Vertically Stacked 2D Perovskite Quantum Wells. *Nat. Commun.* **2018**, *9*, 2130.

(5) Era, M.; Morimoto, S.; Tsutsui, T.; Saito, S. Organic-Inorganic Heterostructure Electroluminescent Device Using a Layered Perovskite Semiconductor $(C_6H_5C_2H_4NH_3)_2PbI_4$. *Appl. Phys. Lett.* **1994**, *65*, 676−678.

(6) Chondroudis, K.; Mitzi, D. B. Electroluminescence from an Organic−Inorganic Perovskite Incorporating a Quaterthiophene Dye within Lead Halide Perovskite Layers. *Chem. Mater.* **1999**, *11*, 3028−3030.

(7) Wang, N.; Cheng, L.; Ge, R.; Zhang, S.; Miao, Y.; Zou, W.; Yi, C.; Sun, Y.; Cao, Y.; Yang, R.; et al. Perovskite Light-Emitting Diodes Based on Solution-Processed Self-Organized Multiple Quantum Wells. *Nat. Photonics* **2016**, *10*, 699−704.

(8) Yuan, M.; Quan, L. N.; Comin, R.; Walters, G.; Sabatini, R.; Voznyy, O.; Hoogland, S.; Zhao, Y.; Beauregard, E. M.; Kanjanaboos, P.; et al. Perovskite Energy Funnels for Efficient Light-Emitting Diodes. *Nat. Nanotechnol.* **2016**, *11*, 872−877.

(9) Gong, X.; Voznyy, O.; Jain, A.; Liu, W.; Sabatini, R.; Piontkowski, Z.; Walters, G.; Bappi, G.; Nokhrin, S.; Bushuyev, O.; et al. Electron−Phonon Interaction in Efficient Perovskite Blue Emitters. *Nat. Mater.* **2018**, *17*, 550−556.

(10) Sutherland, B. R.; Sargent, E. H. Perovskite Photonic Sources. *Nat. Photonics* **2016**, *10*, 295−302.

(11) Eaton, S. W.; Lai, M.; Gibson, N. A.; Wong, A. B.; Dou, L.; Ma, J.; Wang, L.-W.; Leone, S. R.; Yang, P. Lasing Robust Cesium Lead Halide Perovskite Nanowires. *Proc. Natl. Acad. Sci. U.S.A.* **2016**, *113*, 1993−1998.

(12) Zhang, H.; Liao, Q.; Wu, Y.; Zhang, Z.; Gao, Q.; Liu, P.; Li, M.; Yao, J.; Fu, H. 2D Ruddlesden−Popper Perovskites Microring Laser Array. *Adv. Mater.* **2018**, *30*, 1706186.

(13) Qin, C.; Sandanayaka, A. S. D.; Zhao, C.; Matsushima, T.; Zhang, D.; Fujihara, T.; Adachi, C. Stable Room-Temperature Continuous-Wave Lasing in Quasi-2D Perovskite Films. *Nature* **2020**, *585*, 53−57.

(14) Tan, Z.; Wu, Y.; Hong, H.; Yin, J.; Zhang, J.; Lin, L.; Wang, M.; Sun, X.; Sun, L.; Huang, Y.; et al. Two-Dimensional

$(C_4H_9NH_3)_2PbBr_4$ Perovskite Crystals for High-Performance Photodetector. *J. Am. Chem. Soc.* **2016**, *138*, 16612−16615.
(15) Li, W.; Wang, Z.; Deschler, F.; Gao, S.; Friend, R. H.; Cheetham, A. K. Chemically Diverse and Multifunctional Hybrid Organic−Inorganic Perovskites. *Nat. Rev. Mater.* **2017**, *2*, 16099.
(16) Xiao, Z.; Meng, W.; Saparov, B.; Duan, H.-S.; Wang, C.; Feng, C.; Liao, W.; Ke, W.; Zhao, D.; Wang, J.; et al. Photovoltaic Properties of Two-Dimensional $(CH_3NH_3)_2Pb(SCN)_2I_2$ Perovskite: A Combined Experimental and Density Functional Theory Study. *J. Phys. Chem. Lett.* **2016**, *7*, 1213−1218.
(17) Umeyama, D.; Lin, Y.; Karunadasa, H. I. Red-to-Black Piezochromism in a Compressible Pb−I− SCN Layered Perovskite. *Chem. Mater.* **2016**, *28*, 3241−3244.
(18) Castro-Castro, L. M.; Guloy, A. M. Organic-Based Layered Perovskites of Mixed-Valent Gold(I)/Gold(III) Iodides. *Angew. Chem., Int. Ed.* **2003**, *42*, 2771−2774.
(19) Saparov, B.; Mitzi, D. B. Organic−Inorganic Perovskites: Structural Versatility for Functional Materials Design. *Chem. Rev.* **2016**, *116*, 4558−4596.
(20) Smith, M. D.; Crace, E. J.; Jaffe, A.; Karunadasa, H. I. The Diversity of Layered Halide Perovskites. *Annu. Rev. Mater. Res.* **2018**, *48*, 111−136.
(21) Zhu, H.; Miyata, K.; Fu, Y.; Wang, J.; Joshi, P. P.; Niesner, D.; Williams, K. W.; Jin, S.; Zhu, X. Y. Screening in Crystalline Liquids Protects Energetic Carriers in Hybrid Perovskites. *Science* **2016**, *353*, 1409−1413.
(22) Batignani, G.; Fumero, G.; Srimath Kandada, A. R.; Cerullo, G.; Gandini, M.; Ferrante, C.; Petrozza, A.; Scopigno, T. Probing Femtosecond Lattice Displacement Upon Photo-Carrier Generation in Lead Halide Perovskite. *Nat. Commun.* **2018**, *9*, 1971.
(23) Wu, X.; Tan, L. Z.; Shen, X.; Hu, T.; Miyata, K.; Trinh, M. T.; Li, R.; Coffee, R.; Liu, S.; Egger, D. A.; et al. Light-Induced Picosecond Rotational Disordering of the Inorganic Sublattice in Hybrid Perovskites. *Sci. Adv.* **2017**, *3*, No. e1602388.
(24) Bakulin, A. A.; Selig, O.; Bakker, H. J.; Rezus, Y. L. A.; Müller, C.; Glaser, T.; Lovrincic, R.; Sun, Z.; Chen, Z.; Walsh, A.; et al. Real-Time Observation of Organic Cation Reorientation in Methylammonium Lead Iodide Perovskites. *J. Phys. Chem. Lett.* **2015**, *6*, 3663−3669.
(25) Taylor, V. C. A.; Tiwari, D.; Duchi, M.; Donaldson, P. M.; Clark, I. P.; Fermin, D. J.; Oliver, T. A. A. Investigating the Role of the Organic Cation in Formamidinium Lead Iodide Perovskite Using Ultrafast Spectroscopy. *J. Phys. Chem. Lett.* **2018**, *9*, 895−901.
(26) Yaffe, O.; Guo, Y.; Tan, L. Z.; Egger, D. A.; Hull, T.; Stoumpos, C. C.; Zheng, F.; Heinz, T. F.; Kronik, L.; Kanatzidis, M. G.; et al. Local Polar Fluctuations in Lead Halide Perovskite Crystals. *Phys. Rev. Lett.* **2017**, *118*, 136001.
(27) Munson, K. T.; Swartzfager, J. R.; Asbury, J. B. Lattice Anharmonicity: A Double-Edged Sword for 3D Perovskite-Based Optoelectronics. *ACS Energy Lett.* **2019**, *4*, 1888−1897.
(28) Munson, K. T.; Swartzfager, J. R.; Gan, J.; Asbury, J. B. Does Dipolar Motion of Organic Cations Affect Polaron Dynamics and Bimolecular Recombination in Halide Perovskites? *J. Phys. Chem. Lett.* **2020**, *11*, 3166−3172.
(29) Leguy, A. M. A.; Goñi, A. R.; Frost, J. M.; Skelton, J.; Brivio, F.; Rodríguez-Martínez, X.; Weber, O. J.; Pallipurath, A.; Alonso, M. I.; Campoy-Quiles, M.; et al. Dynamic Disorder, Phonon Lifetimes, and the Assignment of Modes to the Vibrational Spectra of Methylammonium Lead Halide Perovskites. *Phys. Chem. Chem. Phys.* **2016**, *18*, 27051−27066.
(30) Quan, L. N.; Park, Y.; Guo, P.; Gao, M.; Jin, J.; Huang, J.; Copper, J. K.; Schwartzberg, A.; Schaller, R.; Limmer, D. T.; et al. Vibrational Relaxation Dynamics in Layered Perovskite Quantum Wells. *Proc. Natl. Acad. Sci. U.S.A.* **2021**, *118*, No. e2104425118.
(31) Koegel, A. A.; Mozur, E. M.; Oswald, I. W. H.; Jalarvo, N. H.; Prisk, T. R.; Tyagi, M.; Neilson, J. R. Correlating Broadband Photoluminescence with Structural Dynamics in Layered Hybrid Halide Perovskites. *J. Am. Chem. Soc.* **2022**, *144*, 1313−1322.
(32) Lin, P. Y.; Loganathan, A.; Raifuku, I.; Li, M. H.; Chiu, Y. Y.; Chang, S. T.; Fakharuddin, A.; Lin, C. F.; Guo, T. F.; Schmidt-Mende, L.; et al. Pseudo-Halide Perovskite Solar Cells. *Adv. Energy Mater.* **2021**, *11*, 2100818.
(33) Liao, C. H.; Chen, C. H.; Bing, J.; Bailey, C.; Lin, Y. T.; Pandit, T. M.; Granados, L.; Zheng, J.; Tang, S.; Lin, B. H.; et al. Inorganic-Cation Pseudohalide 2D $Cs_2Pb(SCN)_2Br_2$ Perovskite Single Crystal. *Adv. Mater.* **2022**, *34*, 2104782.
(34) Nishida, J.; Breen, J. P.; Lindquist, K. P.; Umeyama, D.; Karunadasa, H. I.; Fayer, M. D. Dynamically Disordered Lattice in a Layered Pb-I-SCN Perovskite Thin Film Probed by Two-Dimensional Infrared Spectroscopy. *J. Am. Chem. Soc.* **2018**, *140*, 9882−9890.
(35) Li, C.-H.; Tsai, C.-C.; Liao, M.-Y.; Su, Y.-A.; Lin, S.-T.; Chueh, C.-C. Stable, Color-Tunable 2D SCN-Based Perovskites: Revealing the Critical Influence of an Asymmetric Pseudo-Halide on Constituent Ions. *Nanoscale* **2019**, *11*, 2608−2616.
(36) Hamm, P.; Zanni, M. T. *Concepts and Methods of 2D Infrared Spectroscopy*; Cambridge University Press: New York, 2011.
(37) Kwak, K.; Park, S.; Finkelstein, I. J.; Fayer, M. D. Frequency-Frequency Correlation Functions and Apodization in Two-Dimensional Infrared Vibrational Echo Spectroscopy: A New Approach. *J. Chem. Phys.* **2007**, *127*, 124503.
(38) Kwak, K.; Rosenfeld, D. E.; Fayer, M. D. Taking Apart the Two-Dimensional Infrared Vibrational Echo Spectra: More Information and Elimination of Distortions. *J. Chem. Phys.* **2008**, *128*, 204505.
(39) Kubo, R. A Stochastic Theory of Line Shapes. *Adv. Chem. Phys.* **1969**, *16*, 101−127.
(40) Nishida, J.; Yan, C.; Fayer, M. D. Enhanced Nonlinear Spectroscopy for Monolayers and Thin Films in near-Brewster's Angle Reflection Pump-Probe Geometry. *J. Chem. Phys.* **2017**, *146*, 094201.
(41) Wu, B.; Breen, J. P.; Xing, X.; Fayer, M. D. Controlling the Dynamics of Ionic Liquid Thin Films Via Multilayer Surface Functionalization. *J. Am. Chem. Soc.* **2020**, *142*, 9482−9492.
(42) Daub, M.; Hillebrecht, H. Synthesis, Single-Crystal Structure and Characterization of $(CH_3NH_3)_2Pb(SCN)_2I_2$. *Angew. Chem., Int. Ed.* **2015**, *54*, 11016−11017.
(43) Dang, Y.; Liu, G.; Song, J.; Meng, L.; Sun, Y.; Hu, W.; Tao, X. Layered Perovskite $(CH_3NH_3)_2Pb(SCN)_2I_2$ Single Crystals: Phase Transition and Moisture Stability. *ACS Appl. Mater. Interfaces* **2020**, *12*, 37713−37721.
(44) Glaser, T.; Müller, C.; Sendner, M.; Krekeler, C.; Semonin, O. E.; Hull, T. D.; Yaffe, O.; Owen, J. S.; Kowalsky, W.; Pucci, A.; et al. Infrared Spectroscopic Study of Vibrational Modes in Methylammonium Lead Halide Perovskites. *J. Phys. Chem. Lett.* **2015**, *6*, 2913−2918.
(45) Kenkre, V. M.; Tokmakoff, A.; Fayer, M. D. Theory of Vibrational-Relaxation of Polyatomic-Molecules in Liquids. *J. Chem. Phys.* **1994**, *101*, 10618−10629.
(46) Jones, L. H. Infrared Spectrum and Structure of the Thiocyanate Ion. *J. Chem. Phys.* **1956**, *25*, 1069−1072.
(47) Nakamoto, K. Infrared and Raman Spectra of Inorganic and Coordination Compounds. In *Handbook of Vibrational Spectroscopy*; John Wiley & Sons, Inc.: Hoboken, New Jersey, 2001.
(48) Pérez-Osorio, M. A.; Milot, R. L.; Filip, M. R.; Patel, J. B.; Herz, L. M.; Johnston, M. B.; Giustino, F. Vibrational Properties of the Organic−Inorganic Halide Perovskite $CH_3NH_3PbI_3$ from Theory and Experiment: Factor Group Analysis, First-Principles Calculations, and Low-Temperature Infrared Spectra. *J. Phys. Chem. C* **2015**, *119*, 25703−25718.
(49) Théorêt, A.; Sandorfy, C. The Infrared Spectra of Solid Methylammonium Halides—II. *Spectrochim. Acta, Part A* **1967**, *23*, 519−542.
(50) Yuan, R.; Yan, C.; Tamimi, A.; Fayer, M. D. Molecular Anion Hydrogen Bonding Dynamics in Aqueous Solution. *J. Phys. Chem. B* **2015**, *119*, 13407−13415.
(51) Tan, H.-S.; Piletic, I. R.; Fayer, M. D. Polarization Selective Spectroscopy Experiments: Methodology and Pitfalls. *J. Opt. Soc. Am. B* **2005**, *22*, 2009−2017.

https://doi.org/10.1021/acs.jpcc.2c03516
J. Phys. Chem. C 2022, 126, 10145−10158

(52) Tokmakoff, A. Orientational Correlation Functions and Polarization Selectivity for Nonlinear Spectroscopy of Isotropic Media. I. Third Order. *J. Chem. Phys.* **1996**, *105*, 1−12.
(53) Nishida, J.; Fayer, M. D. Theory of Third-Order Spectroscopic Methods to Extract Detailed Molecular Orientational Dynamics for Planar Surfaces and Other Uniaxial Systems. *J. Chem. Phys.* **2014**, *140*, 144702.
(54) Nishida, J.; Yan, C.; Fayer, M. D. Orientational Dynamics of a Functionalized Alkyl Planar Monolayer Probed by Polarization-Selective Angle-Resolved Infrared Pump−Probe Spectroscopy. *J. Am. Chem. Soc.* **2016**, *138*, 14057−14065.
(55) Lipari, G.; Szabo, A. Model-Free Approach to the Interpretation of Nuclear Magnetic Resonance Relaxation in Macromolecules. 1. Theory and Range of Validity. *J. Am. Chem. Soc.* **1982**, *104*, 4546−4559.
(56) Lipari, G.; Szabo, A. Effect of Librational Motion on Fluorescence Depolarization and Nuclear Magnetic Resonance Relaxation in Macromolecules and Membranes. *Biophys. J.* **1980**, *30*, 489−506.
(57) Wang, C. C.; Pecora, R. Time-Correlation Functions for Restricted Rotational Diffusion. *J. Chem. Phys.* **1980**, *72*, 5333−5340.
(58) Andrews, S. S.; Boxer, S. G. Vibrational Stark Effects of Nitriles I. Methods and Experimental Results. *J. Phys. Chem. A* **2000**, *104*, 11853−11863.
(59) Andrews, S. S.; Boxer, S. G. Vibrational Stark Effects of Nitriles II. Physical Origins of Stark Effects from Experiment and Perturbation Models. *J. Phys. Chem. A* **2002**, *106*, 469−477.
(60) Bagchi, S.; Fried, S. D.; Boxer, S. G. A Solvatochromic Model Calibrates Nitriles' Vibrational Frequencies to Electrostatic Fields. *J. Am. Chem. Soc.* **2012**, *134*, 10373−10376.
(61) Levinson, N. M.; Fried, S. D.; Boxer, S. G. Solvent-Induced Infrared Frequency Shifts in Aromatic Nitriles Are Quantitatively Described by the Vibrational Stark Effect. *J. Phys. Chem. B* **2012**, *116*, 10470−10476.
(62) Nishida, J.; Breen, J. P.; Wu, B.; Fayer, M. D. Extraordinary Slowing of Structural Dynamics in Thin Films of a Room Temperature Ionic Liquid. *ACS Cent. Sci.* **2018**, *4*, 1065−1073.
(63) Bloem, R.; Garrett-Roe, S.; Strzalka, H.; Hamm, P.; Donaldson, P. Enhancing Signal Detection and Completely Eliminating Scattering Using Quasi-Phase-Cycling in 2D IR Experiments. *Opt. Express* **2010**, *18*, 27067−27078.
(64) Hoffman, D. J.; Fayer, M. D. CLS Next Gen: Accurate Frequency−Frequency Correlation Functions from Center Line Slope Analysis of 2D Correlation Spectra Using Artificial Neural Networks. *J. Phys. Chem. A* **2020**, *124*, 5979−5992.
(65) Skinner, J. L.; Hsu, D. Optical and Vibrational Dephasing in Crystals: Theory and Experiment. *J. Lumin.* **1987**, *38*, 134−136.
(66) Skinner, J. L.; Hsu, D. Vibrational Dephasing in Crystals: Theory and Experiment. *Chem. Phys.* **1988**, *128*, 35−45.
(67) Skinner, J. L. Theory of Pure Dephasing in Crystals. *Annu. Rev. Phys. Chem.* **1988**, *39*, 463−478.
(68) Gilman, J. J.; Johnston, W. G. Observations of Dislocation Glide and Climb in Lithium Fluoride Crystals. *J. Appl. Phys.* **1956**, *27*, 1018−1022.
(69) Smith, M. D.; Karunadasa, H. I. White-Light Emission from Layered Halide Perovskites. *Acc. Chem. Res.* **2018**, *51*, 619−627.
(70) Thomaz, J. E.; Lindquist, K. P.; Karunadasa, H. I.; Fayer, M. D. Single Ensemble Non-Exponential Photoluminescent Population Decays from a Broadband White-Light-Emitting Perovskite. *J. Am. Chem. Soc.* **2020**, *142*, 16622−16631.

https://doi.org/10.1021/acs.jpcc.2c03516
J. Phys. Chem. C 2022, 126, 10145−10158